

# Effects of Small Additions of Tin on High-Temperature Oxidation of Fe-Cu-Sn Alloys for Surface Hot Shortness

LAN YIN and SEETHARAMAN SRIDHAR

Steel produced in an electric arc furnace contains a high amount of copper (Cu) that causes a surface-cracking phenomenon called surface hot shortness. It is known that tin (Sn) can exacerbate the hot shortness problem. A series of iron (Fe)-0.3 wt pct Cu- $x$  wt pct Sn alloys with an Sn content ranging from 0.03 to 0.15 wt pct was oxidized in air at 1423 K (1150 °C) for 60 seconds, 300 seconds, and 600 seconds using thermogravimetry. A numerical model developed in a previous article was applied to predict the liquid- $\gamma$ Fe interface concentrations and interface morphology in the Fe-Cu-Sn ternary system. Scanning electron microscopy investigations show that (1) The interface between the oxide and the metal is planar as predicted by the numerical model, (2) Sn leads to severe Cu-rich liquid penetration and cracking along the grain boundaries, and (3) open cracks with Fe oxides were found beneath the oxide-metal interface. The focused ion beam serial-sectioning technique was used to reveal a three-dimensional structure of cracks in the grain boundary containing Cu-rich liquid and Fe oxides.

DOI: 10.1007/s11663-010-9418-9

© The Minerals, Metals & Materials Society and ASM International 2010

## I. INTRODUCTION

ALTHOUGH recycling scrap in electric arc furnaces (EAFs) saves energy, raw material, and cost compared with the conventional blast furnace/basic oxygen furnace (BF/BOF) route,<sup>[1]</sup> surface hot shortness currently limits steel manufacturing via EAF-based techniques.<sup>[2,3]</sup> The feed materials of EAFs are predominantly steel scrap and, thus, inevitably contain copper (Cu), usually between 0.25 wt pct and 0.45 wt pct,<sup>[4]</sup> which mostly originates from scraped cars and electronics parts. When the iron (Fe) in high-Cu residual containing steel oxidizes at temperatures above 1373 K (1100 °C) during the secondary cooling and/or reheating processes, Cu enriches at the oxide-steel interface. Once the content exceeds the Cu solubility in the  $\gamma$ Fe phase, a Cu-rich liquid layer forms, and if it penetrates the  $\gamma$ Fe grain boundaries, then the steel surface will crack during rolling as a result of the weakened grain boundaries. Sometimes, Fe oxides grow on the austenite grain boundary near the oxide- $\gamma$ Fe interface for nickel (Ni)- and silicon (Si)-bearing steel during reheating, which are known as internal oxides.<sup>[5]</sup> Fe oxides also were found inside the cracks after deformation<sup>[6]</sup>; however, it is not known whether these oxides form during the reheating or the rolling processes.

Studies found that a certain amount of tin (Sn) ( $\leq 0.05$  wt pct) and Ni ( $\leq 0.30$  wt pct) always is present in steel scraps along with Cu.<sup>[3,7]</sup> Tin usually comes from

cans and tin-plated steels, whereas nickel originates from alloy steels such as stainless steel.<sup>[3,8]</sup> While Ni is known to ameliorate Cu-induced hot shortness by increasing Cu solubility in the  $\gamma$ Fe phase,<sup>[9]</sup> promoting occlusion<sup>[10]</sup> and decreasing the oxidation rate,<sup>[11]</sup> Sn at contents as low as 0.04 wt pct exacerbates surface hot shortness.<sup>[12,13]</sup> Tin could lower the solubility of Cu in the  $\gamma$ Fe austenite phase<sup>[9]</sup> and lower the melting point of Cu-rich phase.<sup>[14]</sup> A relatively small amount of Sn will counteract the beneficial effect of Ni in the solubility point of view.<sup>[14,15]</sup> It also was found that Sn could promote the penetration of a Cu-rich phase into the grain boundaries,<sup>[16]</sup> but the detailed mechanism through which this occurs is not yet known.

This article focuses on the effects of Sn on the microstructure near the oxide- $\gamma$ Fe interface. Thermogravimetry (TG), scanning electron microscopy (SEM), and focused ion beam (FIB) serial-sectioning techniques were used to investigate oxidation behavior, interface morphology, and three-dimensional (3D) microstructure. A numerical model developed in a previous article<sup>[17]</sup> was applied to support the experimental results, which predicts the liquid- $\gamma$ Fe interface concentrations and interface morphology. An insight on how Sn promotes grain-boundary penetration and cracking is also provided.

## II. METHODOLOGIES

### A. Experimental Methodology

#### 1. Materials

To study the isolated effects of Sn, Fe-Cu-Sn alloys were chosen; the results of Fe, Fe-Cu, and Fe-Cu-Ni alloys also are presented for comparison (all from previous works are marked with asterisks<sup>[11,17]</sup>). It is

LAN YIN, Graduate Student, is with the Department of Materials Science and Engineering, Carnegie Mellon University, Pittsburgh, PA 15213. SEETHARAMAN SRIDHAR, POSCO Professor, is with the Department of Materials Science and Engineering, Carnegie Mellon University, and with the National Energy Technology Laboratory, Pittsburgh, PA 15236. Contact e-mail: sridhars@andrew.cmu.edu

Manuscript submitted April 28, 2010.

Article published online August 10, 2010.

worth mentioning that steels contain carbon (C) and many other impurities. The decarburization could occur parallel with oxidation and cause a decrease in the oxidation rate,<sup>[18]</sup> whereas the presence of oxidizable elements such as Si, aluminum (Al), and manganese (Mn) could promote internal oxides and assist the exclusion of the Cu-rich phase into external scales.<sup>[19]</sup> These elements would therefore likely decrease the enrichment of Cu and Sn at the oxide- $\gamma$ Fe interface. However, to study the isolated effects of Sn on surface hot shortness, it is necessary to exclude the other impurities in the first place. The designed compositions of alloys are listed in Table I. These alloys were produced by the Materials Preparation Center at the Ames Laboratory<sup>[20]</sup> (Ames, IA) through the following procedures: arc melting of the constituent elements in high-purity argon, cold rolled to a thickness of 4 to 5 mm and annealed at 1223 K (950 °C) for 1 hour in vacuum to homogenize the microstructure and remove strain. The ferrite grain size of these samples was approximately 500  $\mu$ m. The chemical analysis of previous Fe, Fe-Cu, and Fe-Cu-Ni alloys produced through the same procedures by Ames Laboratory showed that the relative deviation of the actual contents of major elements (Fe, Cu, and Ni) from the desired values were within 6 pct. C contents were less than 0.02 wt pct, and the other trace elements were less than 10 ppm by mass. The actual chemistries of the designed Fe-Cu-Sn alloys therefore are believed to be reasonably close to the desired values.

## 2. Methods

TG was used to measure the oxidation kinetics of alloys in air at 1423 K (1150 °C) for 60 seconds, 300 seconds, and 600 seconds. One experiment was designed to check the back-diffusion rate of the enriched elements (Cu and Sn) for a 0.6 Sn alloy by annealing the sample in nitrogen for 1 hour after 300 seconds of oxidation. The temperature profile used in the current experiment and TG setup are shown in Figure 1. These samples had the dimensions 19 mm  $\times$  10 mm  $\times$  5 mm and were polished down to 320 SiC abrasive paper before oxidation. Oxidation data were recorded every second and were reported as mass change per unit area ( $\Delta m/A$ ). An infrared gold image furnace with high-energy-density halogen lamps was used to achieve rapid heating. The constant temperature hot zone in the furnace was 14-cm length and 1-cm diameter, and its temperature range was measured to be  $\pm 1$  K. A K-type thermocouple was inserted into the bottom of the tube to measure the hot-zone temperature. Samples were

**Table I. Chemistry of Alloys (in Weight Percent)**

Sample	Fe	Cu	Sn	Ni
Fe	100	0	0	0
Fe-0.3Cu <sup>[11]</sup>	99.70	0.30	0	0
Fe-0.3Cu-0.15Ni <sup>[17]</sup>	99.55	0.30	0	0.15
Fe-0.3Cu-0.03Sn	99.67	0.30	0.03	0
Fe-0.3Cu-0.06Sn	99.64	0.30	0.06	0
Fe-0.3Cu-0.10Sn	99.60	0.30	0.10	0
Fe-0.3Cu-0.15Sn	99.55	0.30	0.15	0

attached to a balance by a platinum wire, and the bottom of the sample was placed as close as possible to the thermocouple to obtain an accurate temperature of the sample. The thermocouple was placed at the point that molten Cu was found (the melting point of Cu 1357 K [1084 °C] is close to the desired temperature). Although the oxidation reaction is exothermic and potentially could heat the sample and the surrounding area, this effect would be counteracted by adjusting the input power of the furnace automatically. As will be shown later, the fact that the isothermal oxidation rate of pure Fe in current set up is consistent with reported values is an in-direct validation for the control of the temperature.

The air flowrate was maintained at 3789 standard cubic centimeters per minute (sccm), corresponding to a linear velocity of 3.22 cm/s at 298 K (25 °C), or 15.25 cm/s at 1423 K (1150 °C), to supply enough oxygen but not to cause sample cooling.<sup>[21,22]</sup> The air used in the oxidation experiments had a water vapor partial pressure of  $1.4 \times 10^{-4}$  atm at 298 K (25 °C).

The samples were cold mounted in epoxy after oxidation to preserve the oxide-metal interfaces and subsequently were sectioned by a low-speed diamond saw. The microstructures of these samples were investigated in a Philips XL30 SEM (Amsterdam, The Netherlands) under a backscatter electron (BSE) mode using a voltage of 25 kV and a working distance of 10 mm. The energy dispersive spectroscopy (EDS) technique was used to confirm the Cu-rich phase and to detect the chemical composition of the liquid phase. The area to be investigated was chosen to be as large as

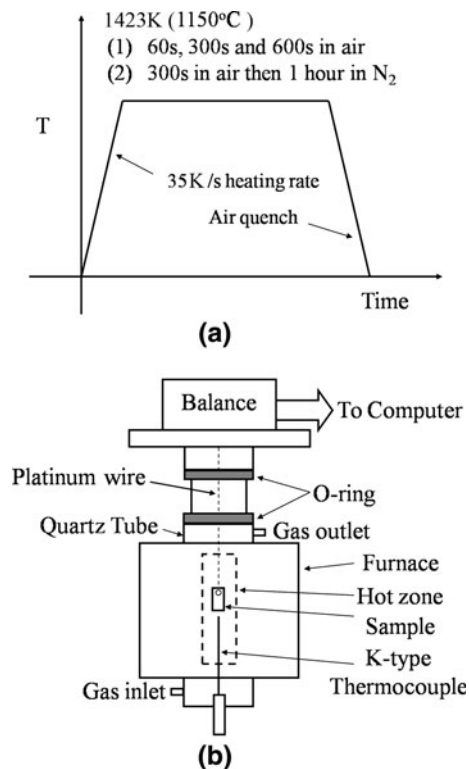


**Fig. 1—(a)** Two types of heating profiles: (1) 60 s, 300 s, and 600 s of oxidation in air and (2) 300 s of oxidation in air followed by 1 h of annealing in N<sub>2</sub>; **(b)** TG setup.

possible to obtain the average concentration of the liquid phase. The normalized liquid–oxide (or oxide– $\gamma$ Fe if no liquid was present) interface roughness was obtained by dividing the tracking interface length at magnification 700 times by the length of the image (195  $\mu\text{m}$ ) to interpret the degree of perturbation from ten SEM images for each chemistry by an open-source software ImageJ.<sup>[23]</sup> The area of the liquid phase was counted by the “wand” function in ImageJ and was normalized to the length of the image for ten images for each sample. The crack length and width were measured for six images of each sample. The crack length was adjusted by adding the thickness of the consumed Fe because part of the crack was incorporated to the external scale because of the recession of the oxide– $\gamma$ Fe interface during oxidation. Standard deviation of the quantification results for each sample was used as a measure of the error.

A FEI NOVA 600 FIB (FEI, Hillsboro, OR) was used to carry out serial sectioning, and the software Amira<sup>[24]</sup> (Visual Concepts GmbH, Berlin, Germany) was used to reconstruct the 3D structure of the liquid phase and open cracks with oxides in the grain boundary.

## B. Modeling Methodology

A numerical model developed in a previous article for the Fe–Cu–Ni system<sup>[17]</sup> was applied to simulate the diffusion process of Sn and Cu in the  $\gamma$ Fe during

oxidation at 1473 K (1150 °C) to compare quantitatively with the experimental results. Interface concentrations and concentration gradients in the  $\gamma$ Fe were calculated as functions of time.

Figure 2(a) shows the arrangement of phases and Sn concentration profiles. The Fe–Cu–Sn phase diagram at 1423 K (1150 °C) was reconstructed by incorporating the Fe–Cu–Sn database from literature<sup>[25]</sup> into the Thermo-Calc (ThermoCalc Software, AB, Stockholm, Sweden) software,<sup>[26]</sup> and the resulting isotherm at 1423 K (1150 °C) is shown in Figure 2(b). The quantities used in the model are summarized in Table II. During the course of oxidation, Cu and Sn would enrich at the oxide– $\gamma$ Fe interface together because they both are nobler than Fe. Therefore, the Cu and Sn interface concentrations at the  $\gamma$ Fe side will increase in the (i) direction as shown in the enlarged view of Figure 2(b) until the concentration reaches the  $\gamma$ Fe–liquid phase boundary. As shown in the Fe–Cu–Sn isotherm, the enrichment of Sn would lower solubility of Cu in  $\gamma$ Fe, which is lowering the required enrichment of Cu for the formation of liquid phase. Once liquid is formed, thermodynamics equilibrium would be set up on both sides of  $\gamma$ Fe–liquid interface, and the  $\gamma$ Fe–liquid interface concentrations can change with time because of the additional degree of freedom in the two-phase region of the Fe–Cu–Sn ternary system. Both Cu and Sn could be incorporated into the liquid phase, which is growing with time, and interface concentrations at both sides

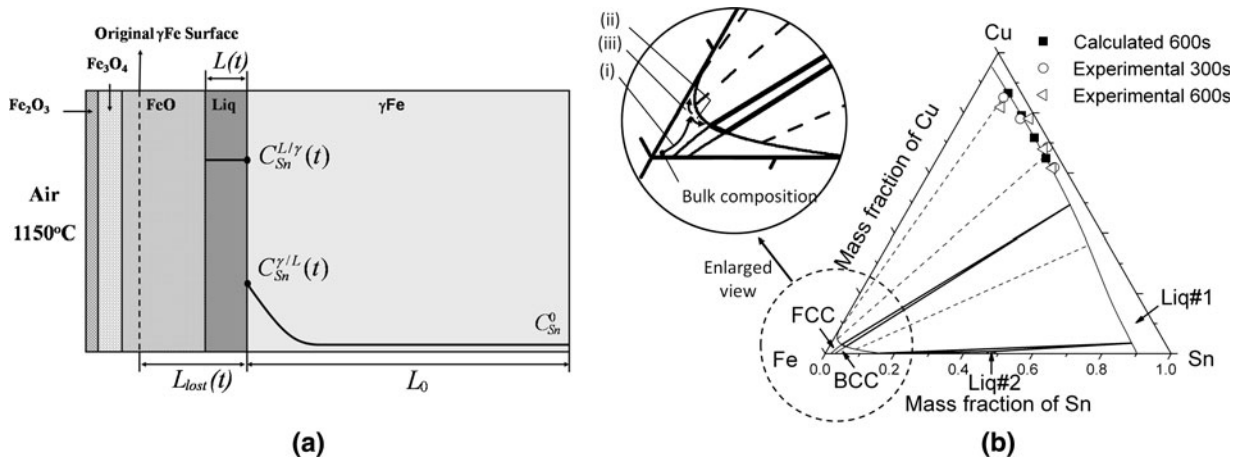


Fig. 2—(a) Phases arrangement and Sn profiles; (b) Fe–Cu–Sn phase diagram at 1423 K (1150 °C) calculated from Thermo-Calc.

Table II. Summary of Quantities

Parameters	Descriptions of Parameters	Nature of Parameters
$L_0$	length of integration zone in $\gamma$ Fe	constant input to the model (m)
$L(t)$	liquid thickness	calculated from the model (m)
$C_i^0$	initial bulk concentration of component $i$	constant input to the model (wt pct)
$C_i^{(\gamma/L)}(t)$	liquid Cu– $\gamma$ Fe interface concentration of component $i$ at the $\gamma$ Fe side	calculated from the model (wt pct)
$C_i^{(L/\gamma)}(t)$	liquid Cu– $\gamma$ Fe interface concentration of component $i$ at the liquid side	calculated from the model (wt pct)
$C_i^\gamma(x, t)$	concentration of component $i$ in the $\gamma$ Fe phase	calculated from the model (wt pct)
$(\Delta m/A)(t)$	mass change per unit area resulting from oxidation	experimental data (mg/cm <sup>2</sup> )
$L_{\text{lost}}(t)$	$\gamma$ Fe thickness lost because of oxidation converted from $(\Delta m/A)(t)$	converted experimental data (m)
$\bar{D}_{ii}^{\text{Fe}}$	lattice interdiffusion coefficient of component $i$ in the Fe matrix	constant input to the model (m <sup>2</sup> /s)

of the  $\gamma$ Fe–liquid interface would change along the phase boundary as oxidation proceeds. In this case, the rejection of Sn because of oxidation has to balance both the incorporation of Sn in the liquid phase and the back diffusion of Sn to the bulk alloy. Therefore, if the rejection rate was small (low Sn alloy or low oxidation rate), then interface Sn concentrations at both sides of the  $\gamma$ Fe–liquid interface would decrease, and the interface concentration would change in the (iii) direction along the phase boundary as shown in Figure 2(b); otherwise, (high Sn alloy or high oxidation rate) Sn would accumulate at the  $\gamma$ Fe side of the  $\gamma$ Fe–liquid interface, and the interface concentration would change in the (ii) direction along the phase boundary in Figure 2(b).

The model was formulated based on the following assumptions:

- Cu-rich liquid formed immediately after oxidation, which was justified by a calculation<sup>[27]</sup> showing that the time for the formation of the liquid phase was about 10 ms.
- The composition of the liquid phase was uniform. Because diffusion in the Cu-rich liquid ( $\sim 10^{-9}$  m<sup>2</sup>/s<sup>[28]</sup>) was rapid compared with diffusion in the oxide ( $\sim 10^{-11}$  m<sup>2</sup>/s<sup>[29]</sup>) and diffusion in  $\gamma$ Fe ( $\sim 10^{-15}$  m<sup>2</sup>/s<sup>[30]</sup>), the concentration gradient across the liquid phase was expected to be shallow. Therefore, the liquid concentrations were assumed to be the same at both liquid– $\gamma$ Fe and liquid–oxide interfaces.
- Nondiagonal terms of ternary interdiffusion coefficients were assumed to be zero, and the on-diagonal terms were assumed to be concentration independent.
- It was assumed that concentration profiles in  $\gamma$ Fe were not distorted by the moving interface when Fe was consumed ( $\gamma$ Fe shrinks) through oxidation.
- The migration of the Cu-rich phase into the scale was negligible. Although reports<sup>[31]</sup> have shown that Cu could migrate into scales in industrial steel samples, our previous work<sup>[32]</sup> showed that this amount was relatively small for Fe-Cu alloys.
- The liquid phase at the oxide– $\gamma$ Fe interface was continuous because the liquid phase would form immediately because of the enrichment of Cu and Sn whenever no liquid coverage was present at the oxide– $\gamma$ Fe interface as long as oxidation kept proceeding (as stated in the first assumption).
- The penetration of liquid down the austenite grain boundaries was not considered because the amount of liquid phase in the grain boundaries was not predictable. The validity of this assumption will be discussed in the modeling results section.

A global mass balance method was adopted in which an integration zone of constant length  $L_0$  was used to integrate the concentration profiles in  $\gamma$ Fe. Fe therefore was considered to be consumed continuously outside the integration zone. The mass balance equations for Cu and Sn are expressed as follows:

$$L(t)C_{\text{Cu}}^{(L/\gamma)}(t) + \int_0^{L_0} C_{\text{Cu}}^\gamma(x, t)dx = (L_0 + L_{\text{lost}}(t))C_{\text{Cu}}^0 \quad [1]$$

$$L(t)C_{\text{Sn}}^{(L/\gamma)}(t) + \int_0^{L_0} C_{\text{Sn}}^\gamma(x, t)dx = (L_0 + L_{\text{lost}}(t))C_{\text{Sn}}^0 \quad [2]$$

To solve Eqs. [1] and [2], the liquid– $\gamma$ Fe interface Cu and Sn compositions on the phase boundaries of the Fe-Cu-Sn ternary phase diagram in both the  $\gamma$ Fe and liquid phases were collected by Thermo-Calc. The transient diffusion model in Comsol Multiphysics (Stockholm, Sweden)<sup>[33]</sup> was applied to solve the diffusion process in  $\gamma$ Fe phase using the finite element method. The following solution strategy was implemented by coupling Comsol Multiphysics and Matlab (Natick, MA)<sup>[34]</sup> to calculate interface concentrations and interface concentration gradients as a function of time:

- Input oxidation TG data, initial interface concentrations and initial liquid thickness
- Obtain the interface Sn concentration that satisfies Eq. [2] (using  $L(t)$  of the last time step)
- Obtain the solution of  $L(t)$  via Eq. [1]
- Repeat steps (b) and (c)

Table III summarizes the input data of the model. The length of the integration zone was chosen to be longer than the diffusion depth of Fe, Cu, and Sn in the  $\gamma$ Fe phase.

The background in regard to interface perturbation was summarized in a previous article.<sup>[17]</sup> At every time instance, the perturbation values were calculated through Eq. [3]<sup>[35]</sup> to predict whether a flat liquid– $\gamma$ Fe interface is stable. The interface was assumed to break down to a nonplanar interface if the perturbation criterion value was negative. Equation [3] is expressed as follows:

$$m^\gamma(t)G_{\text{Sn}}^{(\gamma/L)}(t) - G_{\text{Cu}}^{(\gamma/L)}(t) < 0 \text{ (nonplanar interface)} \quad [3]$$

where  $G_{\text{Sn}}^{(\gamma/L)}(t)$  and  $G_{\text{Cu}}^{(\gamma/L)}(t)$  are concentration gradients for Sn and Cu, respectively, on the  $\gamma$ Fe side of the liquid– $\gamma$ Fe interface, assuming a flat interface. As shown in Figure 2(a), with the positive direction from the oxide to the  $\gamma$ Fe phase, both  $G_{\text{Sn}}^{(\gamma/L)}(t)$  and  $G_{\text{Cu}}^{(\gamma/L)}(t)$  would be negative. The slope of the liquid– $\gamma$ Fe phase boundary at the  $\gamma$ Fe side at certain time  $m^\gamma(t)$  was obtained by curve fitting data from Thermo-Calc.

**Table III. Input Values**

Values of Parameters	Description of Parameters
$L_0 = 25 \mu\text{m}$	length of integration zone in $\gamma$ Fe
$\tilde{D}_{\text{CuCu}}^{\text{Fe}} = 2.66 \times 10^{-15} \text{ m}^2/\text{s}$	lattice diffusivity of Cu in matrix $\gamma$ Fe <sup>[30]</sup>
$\tilde{D}_{\text{SnSn}}^{\text{Fe}} = 2.10 \times 10^{-14} \text{ m}^2/\text{s}$	lattice diffusivity of Sn in matrix $\gamma$ Fe <sup>[30]</sup>
$C_{\text{Sn}}^0$ and $C_{\text{Cu}}^0$	initial bulk concentration of Sn and Cu
$L_{\text{lost}}(t)$	$\gamma$ Fe thickness lost resulting from oxidation



### III. RESULTS AND DISCUSSION

#### A. TG Results

Figure 3(a) shows TG curves ( $\Delta m/A$  vs time) for pure Fe and Fe-Cu-Sn alloys. Fe-0.3 wt pct Cu<sup>[11]</sup> and Fe-0.3 wt pct Cu-0.15 wt pct Ni<sup>[17]</sup> TG results from previous works also are provided for comparison. The SEM characterization and analysis of these samples were carried out independently in the current work. As shown in Figure 3(a), all TG curves obeyed a linear rate law in the first 50 to 110 seconds and subsequently changed to a parabolic rate law after approximately 180 seconds. Measured linear and parabolic oxidation rate constants are summarized in Figure 4. Linear rate constants were obtained by linear fitting ( $\Delta m/A$  vs time) of the first 50 seconds (0.15Ni alloy), 60 seconds (Fe and Fe-Cu-Sn alloys), or 110 seconds (Fe-Cu alloy) data as shown in Figure 3(b). The slight change of linear rate shown in Figure 3(b) could result from the scattering of experimental data. Parabolic fitting ( $(\Delta m/A)^2$  vs time) was conducted for different time intervals after the linear regime, and the fitting parabolic rate became stable after 180 seconds in most case, which suggested that beyond 180 seconds the oxidation changed to the parabolic stage. The parabolic rate constants then were given by parabolic fitting of data after 180 seconds to avoid the transition region as given in Figure 3(c) (the squares of correlation coefficient  $r^2$  of these fittings are between 0.99 and 1.00). The treatment

of all data was consistent to ensure that the rate constants were comparable. The calculated linear<sup>[22]</sup> and parabolic rate constants from regression of literature data<sup>[36]</sup> for pure Fe in air at 1423 K (1150 °C) are presented as straight lines in Figure 4. The equations and parameters for calculating the linear rate constant<sup>[22]</sup> were shown in a previous article,<sup>[17]</sup> and the bulk flow term was taken into account. These results show that the linear oxidation rates for all alloys were similar, which is reasonable because in this regime, the oxidation rates would be expected to be controlled by gas-phase transfer of oxygen instead of the dissociation of molecular oxygen on the surface<sup>[18]</sup> and were independent of alloy chemistry.<sup>[22]</sup> The parabolic rate was expected to be controlled by Fe cation diffusion through the wüstite layer.<sup>[37]</sup> The parabolic rate constants for Fe-Cu-Sn alloys were observed to be lower than the Fe and Fe-Cu cases and yet a little higher than the 0.15Ni alloy (Figure 4(b)). This will be discussed briefly later on. The reduction of surface area after oxidation was estimated to be less than 9 pct; thus, a constant surface area was assumed in the analysis.

#### B. SEM Results

The interface microstructure was observed under SEM for all alloys after oxidation, and the results are shown in Figure 5. The oxide layers are not visible in some images because the oxides of the samples separated

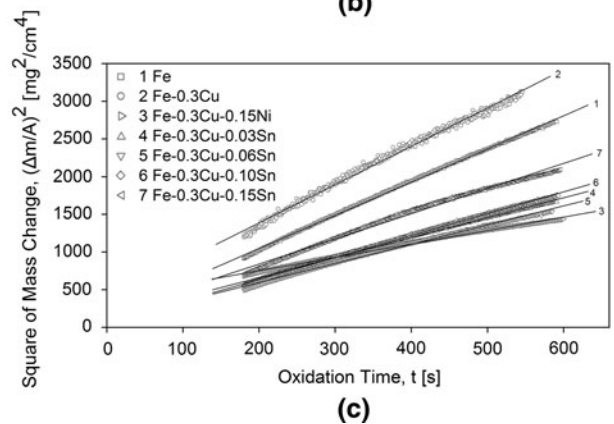
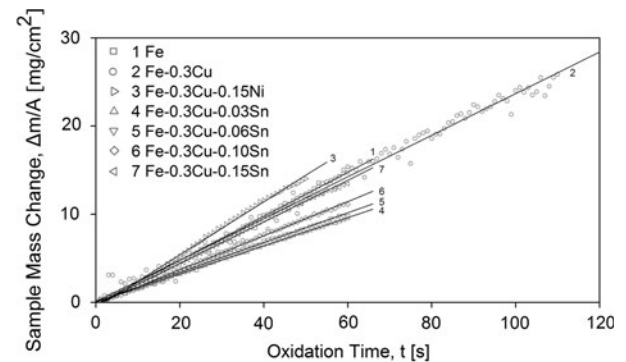
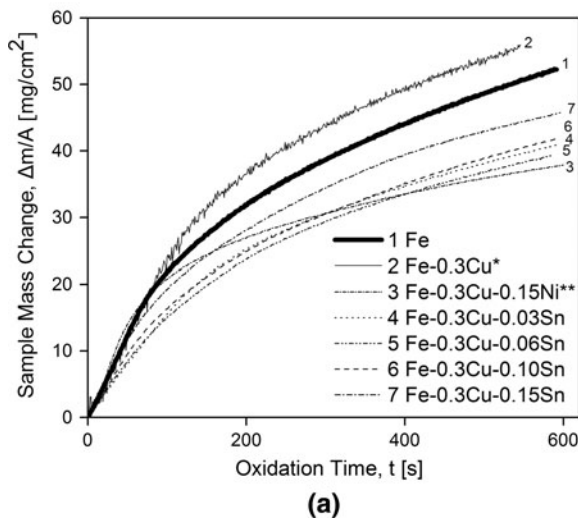


Fig. 3—Oxidation behavior of samples oxidized for 600 s. (a) TG-measured weight change; (b) linear fitting; (c) parabolic fitting, \*Ref. 11; \*\*Ref. 17.

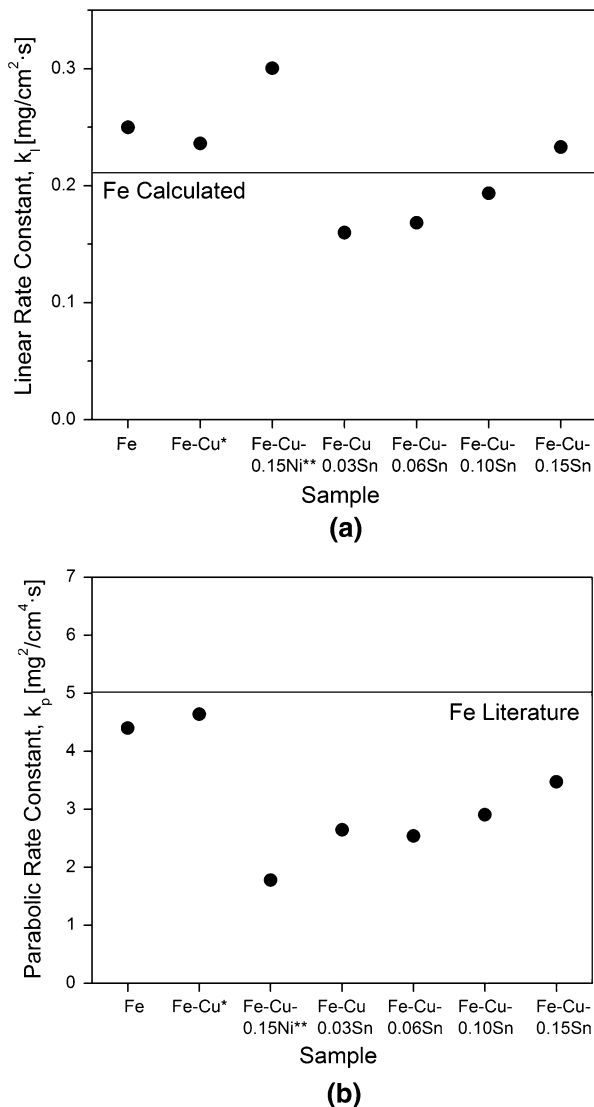


Fig. 4—(a) Linear oxidation rate constants; (b) parabolic oxidation rate constants, \*Ref. 11; \*\*Ref. 17.

from the metal after cooling in air. Unlike the other ternary system Fe-Cu-Ni, which showed a wavy oxide- $\gamma$ Fe interface, the interface of Fe-Cu-Sn alloys remained planar (like the Fe and Fe-Cu alloys), which is illustrated in Figure 6(a). Few internal oxides were found near the liquid phase for Fe-Cu-Sn alloys compared with Fe-Cu-Ni alloys. Significantly more Cu-rich phase was present in the grain boundaries for Fe-Cu-Sn alloys compared with the other alloys (Fe-Cu and Fe-Cu-Ni), as shown in Figure 5. It also is shown that the continuous Cu-rich layer in the Fe-Cu alloy (Figure 5(b)) became sparse liquid droplets at the oxide- $\gamma$ Fe interface when Sn was added, which could result from the fact that a large amount of liquid phase went into grain boundaries or a difference in the wetting behavior of Sn containing Cu-rich phase on the  $\gamma$ Fe phase. Fe oxides were also observed along the open cracks in the grain boundaries in all Fe-Cu-Sn alloys. These oxides were believed to be wüstite at 1423 K (1150 °C) because they

were formed in a Fe-rich environment. Interestingly, the liquid phase always was present at the end of the crack, and the wüstite were seldom found along the grain boundary cracks where liquid coverage was noted. Before showing subsequent results, it is first worth mentioning that the words “penetration/wetting” and “crack” frequently present in different literature do not have consistent meaning, which is confusing. On the one hand, in the current article, “penetration/wetting” refer to the nanometers thickness of liquid present in the grain boundary, which is not visible in SEM images. On the other hand, “crack” refers to the broadened grain boundary, like a channel with micrometers width, which could be filled with liquid phase or stay open. Therefore, the visible liquid phase and open cracks in the grain boundaries in Figure 5, henceforth in this article, are referred to as cracks. The width and length of cracks for Fe-Cu-Sn alloys are summarized in Figures 6(b) and (c). The crack length increased as oxidation proceeds, but the crack width did not change much with time. It could be noted that the variations in both crack length and width was large, and therefore, no evident trend can be drawn between different Sn contents. This variation is foreseeable because liquid penetration and broadening likely will depend on the grain-boundary character of polycrystals.<sup>[38]</sup>

### C. FIB Serial Sectioning

Figure 7 shows the FIB serial sectioning and 3D reconstruction of the liquid phase and Fe oxides along the crack. Wüstite was observed clearly along the cracks at locations where no liquid phase was present. It is shown (as was shown in the two-dimensional [2D] images in Figure 5) that the crack either was full of liquid phase or was filled with liquid phase at the end with oxides growing along the open crack on the top (as shown in Figure 7(c)).

### D. Modeling Results

As shown in Figure 5, a significant amount of liquid phase entered grain boundaries, but it was ignored in this simplified model. Nevertheless, although the values of interface concentrations could be different (as will be discussed subsequently), the simplified model is expected to give a reasonable trend of interface concentrations among different Sn-containing alloys because the calculation for each case was made under the same assumption.

The evolution of Sn interface concentrations  $C_{\text{Sn}}^{(\gamma/L)}$  and  $C_{\text{Sn}}^{(L/\gamma)}$  are shown in Figure 8. According to the modeling results, once liquid formed at the oxide- $\gamma$ Fe interface,  $C_{\text{Sn}}^{(\gamma/L)}$  increased for the 0.15 Sn alloy, whereas it decreased for the other Sn alloys because of the higher Sn rejection rate of the 0.15 Sn alloy (high bulk Sn content and similar oxidation rate with other Sn alloys). It also is noted that  $C_{\text{Sn}}^{(\gamma/L)}$  stopped changing after 30 seconds because the liquid phase can incorporate a large amount of Sn and the diffusivity of Sn is large; therefore, the rejected Sn could be balanced by a small change of the back diffusion flux of Sn, and the rest is incorporated in the liquid phase. Therefore, changes in

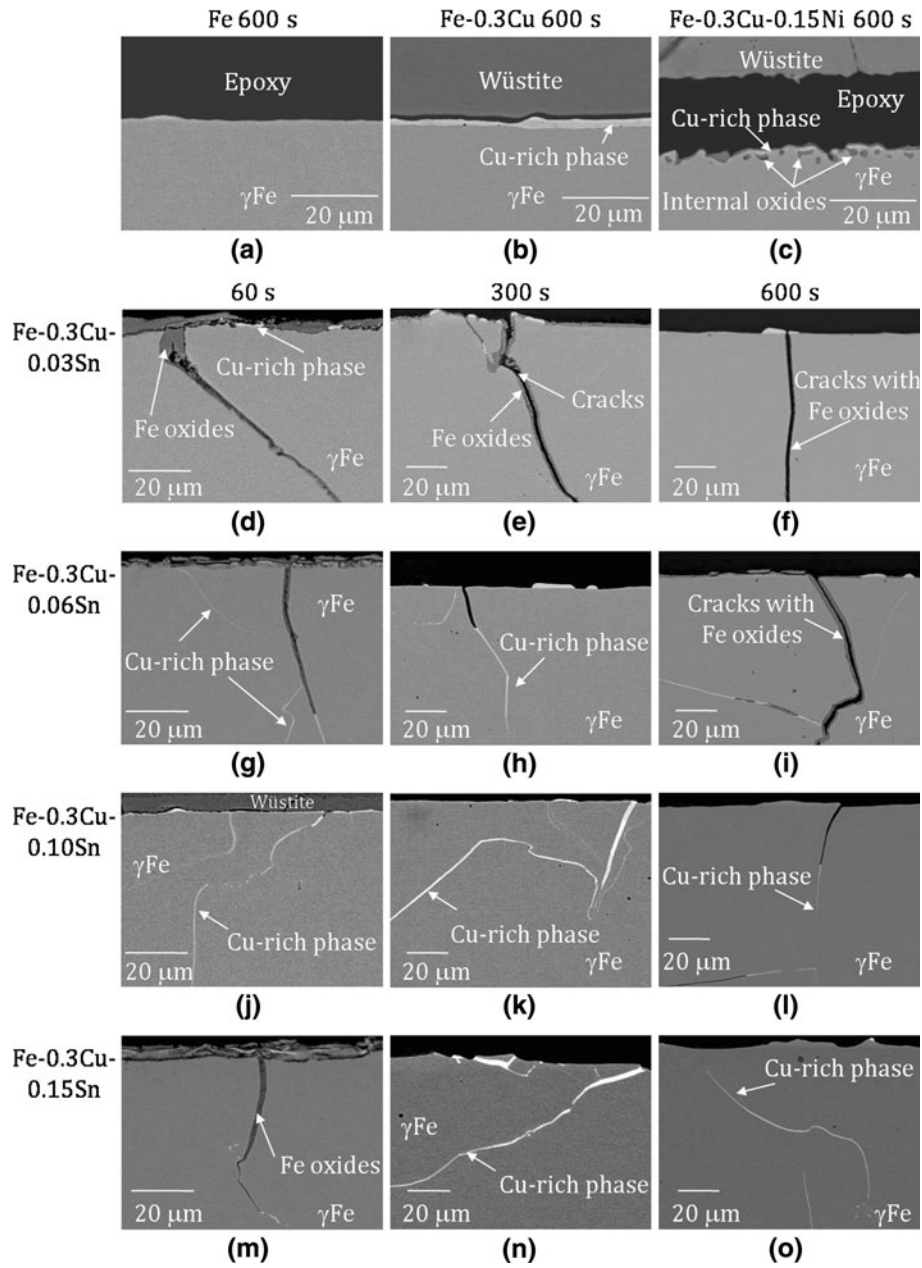


Fig. 5—BSE-SEM images of oxide- $\gamma$ Fe interface.

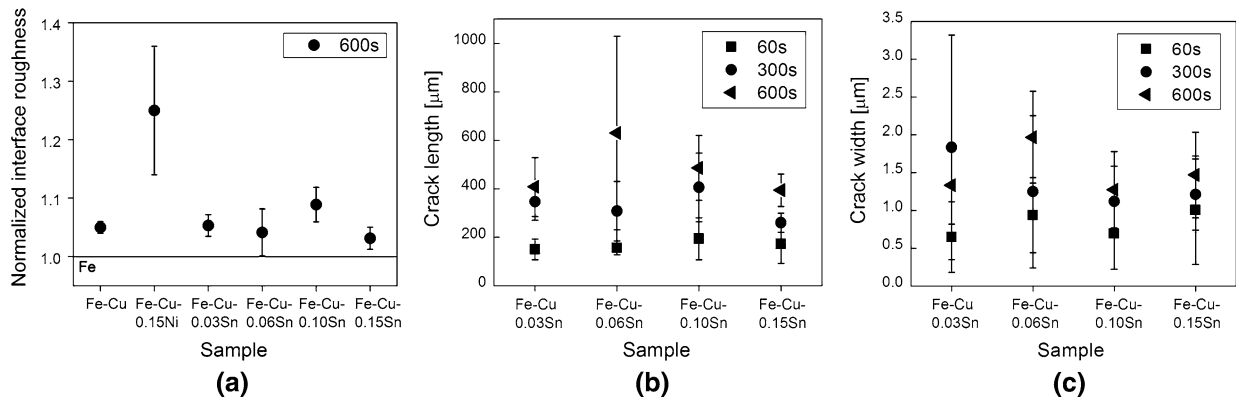


Fig. 6—(a) Normalized interface roughness; (b) crack length; (c) crack width.

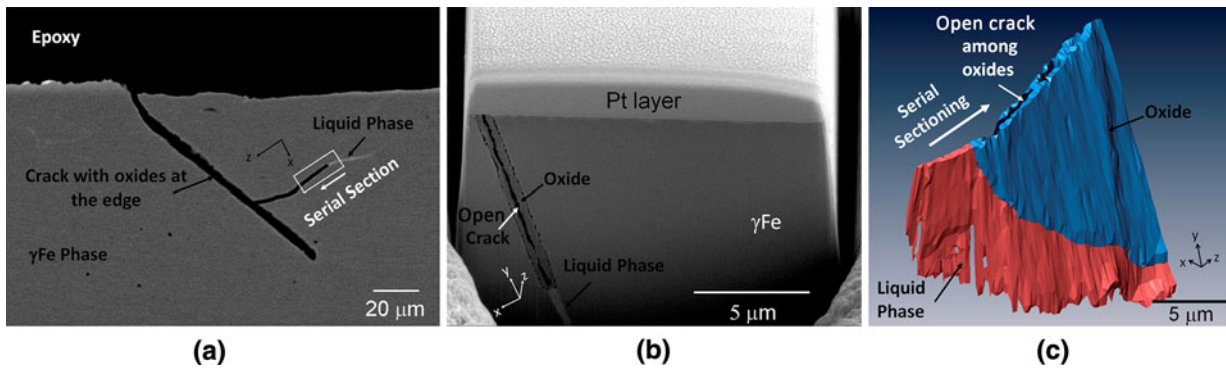


Fig. 7—FIB serial sectioning. (a) The position for serial sectioning in the 2D BSE image; (b) Serial sectioning in FIB; (c) 3D reconstruction of liquid phase and cracks after serial sectioning. (color online).

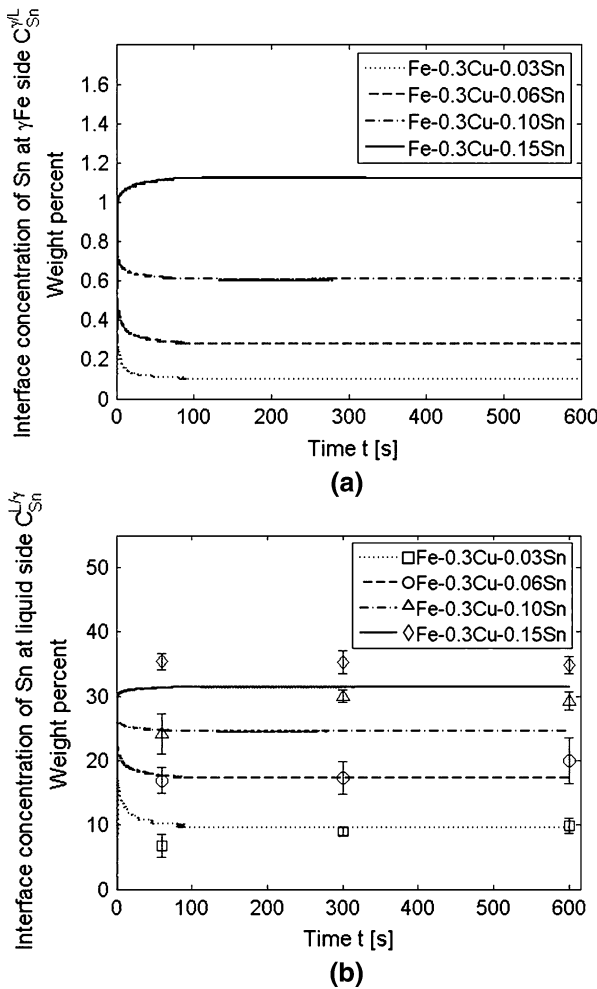


Fig. 8—(a) Computed evolution of the Sn interface concentration at the  $\gamma\text{Fe}$  side.  $C_{\text{Sn}}^{\gamma/L}$ ; (b) Computed evolution of the Sn interface concentration at the liquid side  $C_{\text{Sn}}^{L/\gamma}$  and experimental interface concentrations.

the Sn interface concentration become smaller and smaller and eventually stop because of the back diffusion of Sn to the bulk, and the incorporation of Sn in the liquid phase balances the rejection of Sn without changing the interface concentrations. The calculated  $\gamma\text{Fe}$ –liquid interface concentrations at the

liquid side of Cu, Sn, and interface concentrations at the  $\gamma\text{Fe}$  side of both Cu and Sn after 600 seconds of oxidation are shown in Figures 9(a) through (c) respectively. A higher bulk Sn content resulted in a higher Sn interface concentration but with a lower Cu interface concentration.

SEM-EDS results were collected by averaging the concentrations in the liquid phase at the  $\gamma\text{Fe}$ –oxide interface from six areas for each sample and are shown in Figures 8(b), 9(a) and (b). The concentrations in the liquid phase were assumed to be identical to the liquid– $\gamma\text{Fe}$  interface concentration at the liquid side because the concentrations were believed to be uniform across the liquid phase resulting from the fast liquid diffusivity as stated in the second assumption in the modeling methodology section. The calculated interface concentrations and EDS results for 300 seconds and 600 seconds also are plotted on the phase diagram in Figure 2(b). The measured EDS results for 60 seconds, 300 seconds, and 600 seconds were reasonably similar, which validated the calculated results that interface concentration stayed constant after some time. Some larger deviations of the 60-seconds findings resulted from the thin liquid layer considering the interaction volume of the X-ray. Liquid droplets for 300 seconds and 600 seconds were large enough to give accurate concentrations in the liquid phase. Both calculated concentrations and the measured EDS results showed the same trend that a higher bulk Sn content results in a higher Sn interface concentration and in a lower Cu interface concentration in the liquid phase, and the concentration values were reasonably close (Figure 8(b)). In the real case, because of the entrance of liquid into grain boundaries, less Sn could be incorporated in the liquid remaining at the oxide– $\gamma\text{Fe}$  interface. Therefore, more Sn could enrich at the  $\gamma\text{Fe}$  side, resulting in a higher Sn interface concentration and therefore in a lower Cu interface concentration on both sides of the  $\gamma\text{Fe}$ –oxide interface compared with the simplified model. However, the entrance of liquid phase into the grain boundaries is not expected to change the interface concentrations much because, as shown in Figure 8(b), the interface concentrations would stop changing within a short time, indicating that Sn does not enrich strongly at the interface, and once liquid forms, the interface



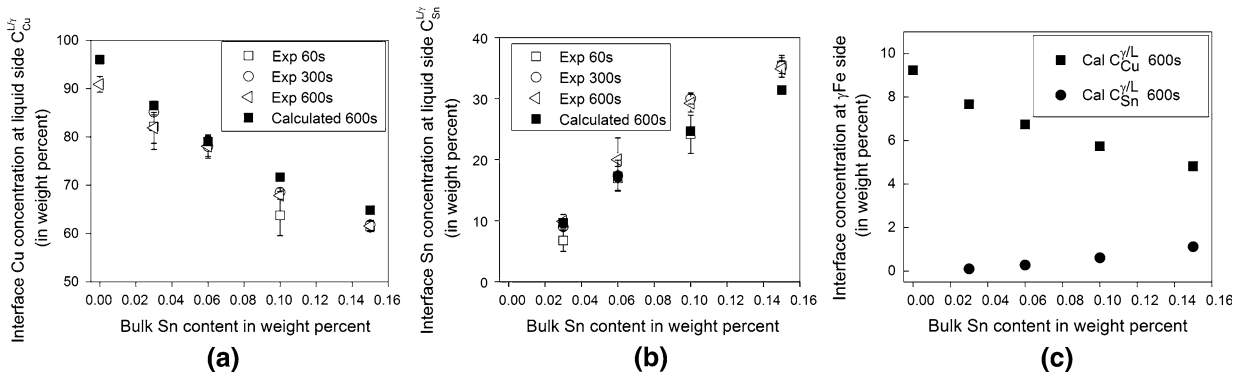


Fig. 9—Experimental and calculated interface concentrations for Fe-Cu and Fe-Cu-Sn alloys at both the  $\gamma$ Fe and liquid sides.

concentrations do not need to change much to satisfy the mass balance. Therefore, it will not make a big difference whether the liquid phase stays at the  $\gamma$ Fe–oxide interface or enters the grain boundaries. The reasonable match between experiments and predictions suggested that the amount of Cu that went into the grain boundaries was not sufficient to cause a big discrepancy. The concentrations of liquid phase in the grain boundaries also were investigated. However, because of the thin liquid layer and the unpredicted liquid channel beneath the viewed surface, results always showed a higher Fe concentration, which was a sign that data from the Fe matrix also contributed to the EDS results. Nevertheless, for some grain boundary liquid regions that did show reasonable Fe concentrations, the liquid concentrations were similar to those at the  $\gamma$ Fe–oxide interface because of the small back diffusion flux as will be shown later. Moreover, the predicted liquid thickness in the model for Fe-Cu-Sn alloys oxidized for 600 seconds was around 0.5  $\mu$ m, which was similar to the liquid thickness of the Fe-Cu case because although the oxidation rate of the Fe-Cu alloy was faster than that of the Fe-Cu-Sn alloys (resulted in a faster rejection rate), the liquid phase in the Fe-Cu-Sn alloys can incorporate a significant amount of Sn as shown in Figure 9(b), and the back diffusion of Cu was smaller because of a lower interface Cu concentration in the  $\gamma$ Fe phase (Figure 9(c)) that counteracted the oxidation effects.

The modeling results also showed that the perturbation value  $m^\gamma(t)G_{Sn}^{(\gamma/L)}(t) - G_{Cu}^{(\gamma/L)}(t)$  was always positive, suggesting a planar interface is stable. This was expected because of the nature of the Fe-Cu-Sn phase boundary, of which  $m^\gamma(t)$  in the low Sn part was always negative (Figure 2(b)) as well as  $G_{Sn}^{(\gamma/L)}(t)$  and  $G_{Cu}^{(\gamma/L)}(t)$ . Therefore, the perturbation values remained positive. This prediction was consistent with the experimental SEM results shown in Figure 6(a). Although, as shown in the previous article, the perturbation values calculated for the Fe-Cu-Ni system showed negative values with a sufficient bulk Ni content (around 0.06 wt pct), which also matched the SEM observation.<sup>[17]</sup> Sn and Ni clearly played different roles in contributing to interface morphology.

To summarize, despite the presence of a large amount of liquid in the grain boundaries, the model still could

predict reasonably the liquid concentration at the  $\gamma$ Fe–wüstite interface and interface morphology.

### E. Grain-Boundary Wetting

The results in Figure 5 indicated that a significant amount of Cu-rich liquid entered the grain boundaries when Sn was present, which also has been noted by some previous researchers.<sup>[16,39]</sup> The mechanism governing liquid-metal penetration into a solid metal matrix (wetting) and a broadening grain boundary without applied stress has not yet been fully understood.<sup>[40,41]</sup> It is known that a liquid phase would tend to wet the grain boundary if it would lower the interfacial grain boundary energy.<sup>[42]</sup> Although such a thermodynamic driving force would not favor liquid thickness beyond several nanometers<sup>[41]</sup> (e.g., the micrometer width channel shown in Figure 5), it has been reported that wetting of the grain boundary at the crack tips was crucial for crack initiation and later crack propagation (grain-boundary broadening).<sup>[43,44]</sup> The fact that the Cu-rich liquid always was present at the crack tip (Figure 5) provided an indication that the presence of liquid was important for crack formation. Therefore, the effects of Sn on the liquid wetting behavior will be discussed in terms of interfacial tension, internal stress, and vacancy condensation.

#### 1. Interfacial tension

A dihedral angle  $\theta_0$  in the current case is defined by the balance of interfacial tension between the Fe and the liquid phase,  $\gamma_{Fe/L}$  and by interfacial tension between the Fe grain boundaries  $\gamma_{Fe/Fe}$  according to  $\gamma_{Fe/Fe} = 2\gamma_{Fe/L} \cos(\theta_0/2)$ . If  $\gamma_{Fe/Fe} \geq 2\gamma_{Fe/L}$  ( $\theta_0$  equals zero), then the liquid phase will form a continuous layer along the grain boundaries. Otherwise, liquid still could penetrate until the predicted equilibrium dihedral angle is met. Sn is known to segregate along grain boundaries in an Fe-Sn alloy.<sup>[45]</sup> Therefore, it could be hypothesized that Sn might lower the interfacial tension  $\gamma_{Fe/L}$  and the dihedral angle as well. Salter,<sup>[9]</sup> however, showed that Sn actually increased the dihedral angle slightly but not enough to prevent grain-boundary penetration. The observations in the current experiments indicated that the liquid phase on a low Sn alloy (Figure 10(a)) or on a

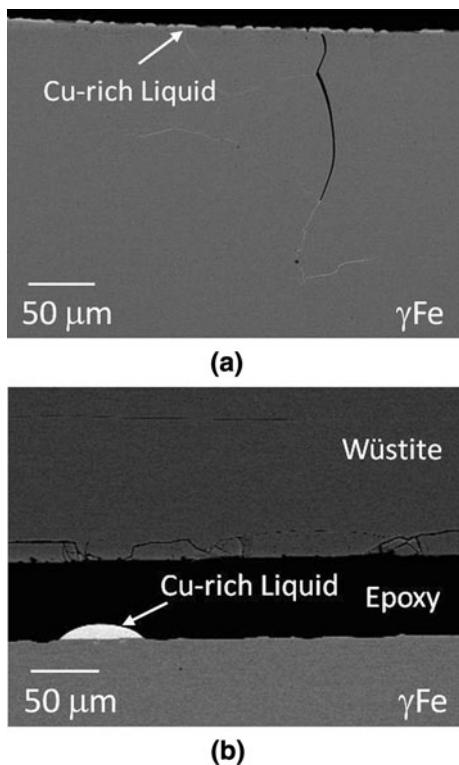


Fig. 10—BSE-SEM images of oxide- $\gamma$ Fe interface. (a) 0.03 Sn alloy of 600 s oxidation; (b) 0.15 Sn alloy of 600 s oxidation.

zero Sn alloy (Figure 5(b)) tended to spread along the oxide- $\gamma$ Fe interface, whereas the liquid phase tended to segregate as a big droplet for a high Sn alloy (Figure 10(b)). However, this phenomenon likely results from the cooling process, which might not indicate the real wetting potential of Sn containing liquid on Fe. Glickman and Nathan<sup>[40]</sup> suggested that instead of the equilibrium angle  $\theta_0$ , a minimum dynamic angle  $\theta_d$  (greater than  $\theta_0$ ) was established at the crack tip during the wetting process. Glickman and Nathan's<sup>[40]</sup> argument is plausible because as long as liquid keeps penetrating the grain boundary, the equilibrium dihedral angle is not likely reached. In current experiments, although it is hard to identify the end of a liquid channel in 2D images, the dihedral angle was estimated to be 8.3 deg, averaging from ten images, which is an indication that  $\theta_d$  has not yet reached 0 deg. Although the equilibrium angle  $\theta_0$  is not known in current experiments, it is possible that  $\theta_0$  has not yet been reached because liquid phase kept propagating along grain boundaries. The dihedral angle data in the literature mentioned might have been obtained under dynamic, rather than equilibrium, conditions and therefore might not indicate the interfacial tension. The effect of Sn on capillarity thus cannot be established unambiguously.

## 2. Internal stress

During the course of oxidation, the oxides formed on the metal will create compressive stress because of the difference in volume of Fe oxides and Fe.<sup>[18]</sup> However, the stress induced by external oxides was believed to be almost the same for Fe-Cu, Fe-Cu-Ni, and Fe-Cu-Sn

alloys, and hence, this could not explain the significant penetration promoted by Sn.

As mentioned in Section III-E-1, Glickman and Nathan<sup>[40]</sup> suggested that a dynamic angle  $\theta_d$  (greater than  $\theta_0$ ) was established at the crack tip.<sup>[40]</sup> Therefore, a stress could be generated pointing to the solid. Because the Cu-rich liquid phase already was saturated with Fe during the enrichment process, instead of helping remove solid Fe atoms from the tip, this stress could help insert liquid atoms into the grain boundaries. According to the data in literature, the  $\gamma$ Fe grain boundary impurity diffusivity of Sn ( $s\delta D_b = 1.11 \times 10^{-17} \text{ m}^2/\text{s}$ )<sup>[46]</sup> is likely to be faster than Cu ( $s\delta D_b = 9.54 \times 10^{-19} \text{ m}^2/\text{s}$ )<sup>[47]</sup> where  $s$  is the segregation factor (assumed to be 1 for such a high temperature and a short experimental time) and  $\delta$  is the grain-boundary thickness (assumed to be equal for all alloys). The presence of Sn in the liquid phase therefore could help insert liquid atoms into grain boundaries. Nam and Srolovitz also suggested that faster grain-boundary diffusivity could help dislocation climb down, which assisted the penetration propagation.<sup>[48]</sup> Sigle *et al.* pointed out that the grain boundary would be weakened after inserting three layers of liquid atoms because of the weakened bonds among liquid atoms, which enhanced the tendency for grain-boundary sliding and the formation of liquid channel thereafter.<sup>[49]</sup> The bonds between Sn-Sn are believed to be much weaker than the bonds between Cu-Cu, which is related to the significantly lower melting point of Sn. It then can be speculated that the presence of Sn in the grain boundaries would assist the gliding of a grain boundary and therefore the later formation of channel and broadening of a grain boundary. In all, the stress-induced diffusion of the Sn atom in the grain boundaries and the weak bond strength could result in significant grain-boundary penetration.

## 3. Condensation of vacancy

It has been reported that diffusion along a grain boundary could cause Kirkendall porosity<sup>[50]</sup> near the grain boundary, which might assist grain-boundary penetration of liquid films.<sup>[51]</sup> Fredriksson *et al.*<sup>[52]</sup> proposed that although liquid Cu diffused to  $\gamma$ Fe grain boundaries, the lateral diffusion of Cu through the grain boundaries could cause vacancies condensation, which was responsible for the propagation and broadening of the liquid layer in the grain boundaries. Although the impurity diffusivity of Sn in matrix Fe ( $2.10 \times 10^{-14} \text{ m}^2/\text{s}$ ) is much faster than the self-diffusivity of Fe ( $1.56 \times 10^{-15} \text{ m}^2/\text{s}$ ) and the impurity diffusivity of Cu ( $2.66 \times 10^{-15} \text{ m}^2/\text{s}$ ),<sup>[30]</sup> the interface concentration of Sn at the  $\gamma$ Fe side was expected to be small as shown in Figure 9(c), and therefore, the resulting back-diffusion flux of Sn is consequently small. According to the modeling results, the Cu interface concentration would be lower in the presence of Sn, and therefore, the flux of Cu would be smaller for the Fe-Cu-Sn alloys compared with the Fe-Cu cases as well. Back-diffusion fluxes of neither Sn nor Cu was expected to be great compared with the Fe-Cu case, and thus, the vacancy condensation theory cannot explain the penetration

promoted by Sn. The slow back diffusion of liquid phase was confirmed by a test in which 0.06 Sn alloy was oxidized in air for 300 seconds at 1423 K (1150 °C) and then annealed in N<sub>2</sub> for 1 hour at the same temperature. The TG data showed that oxidation stopped (as would be expected) after switching gas from air to N<sub>2</sub>. The quantification of the amount of liquid phase for the 0.06 Sn alloy with or without annealing in N<sub>2</sub>, however, does not vary much, as shown in Figure 11, suggesting that the back-diffusion flux was indeed negligible for the time period in current experiments. Calculations based on the formulas in Fredriksson *et al.*'s article<sup>[52]</sup> with the interface concentrations in the current experiment assuming a binary diffusion process (either Cu or Sn play the major role) resulted in a much smaller width (~0.05 μm) and length (~50 μm) of the cracks than the experimental observation (Figures 6(b) and (c)). Moreover, no porosity was observed at the liquid-γFe interface in the grain boundary in the FIB results (Figure 7(b)). Thus, the vacancy condensation mechanism may not, at least by itself, account for the observed significant penetration caused by Sn in the current study.

After reviewing the aforementioned possible liquid penetration mechanisms, the following properties of Sn are believed to affect penetration: (1) the fast grain

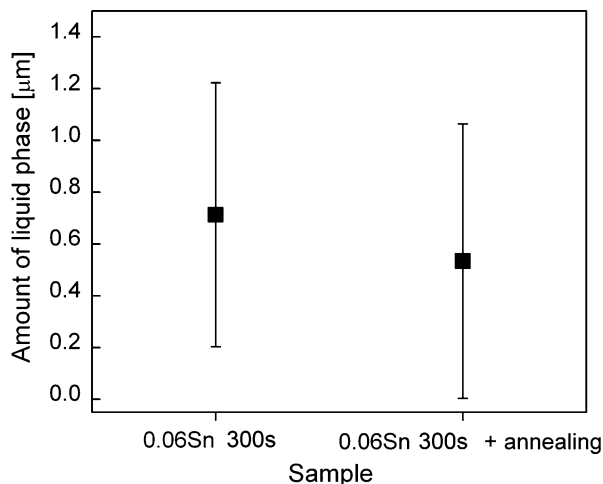


Fig. 11—The amount of liquid phase for 0.06 Sn alloy oxidized for 300 s with and without annealing.

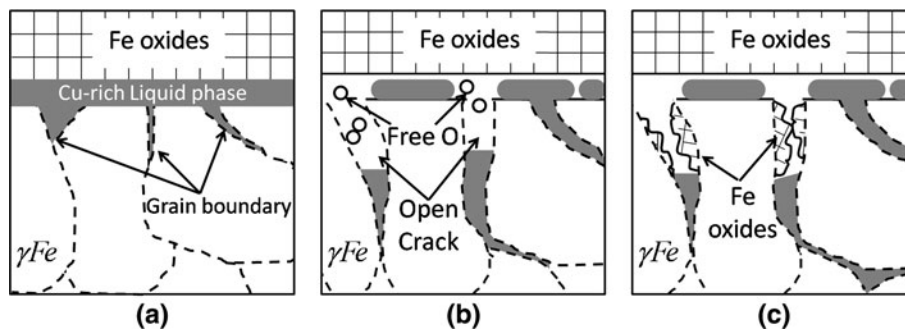


Fig. 12—Mechanism for oxide formation at the open cracks in the grain boundary.

boundary diffusivity, which helps insert atoms into a grain boundary in the presence of internal stress and (2) the weak bonds, which facilitates grain-boundary gliding. These properties could result in significant grain-boundary penetration and in later broadening in the presence of Sn.

#### F. Oxide Formation in Open Cracks

It was shown in the SEM and FIB results that wüstite was formed along the open cracks in the grain boundaries. Interestingly, these oxides formed where no liquid phase was present as shown in the FIB serial-sectioning images (Figure 7(b)). A speculation on the formation of oxides at the open cracks in the grain boundaries is shown in Figure 12. First, the significant liquid penetration and grain-boundary broadening are promoted in the presence of Sn. Although the liquid phase keeps filling into the channel in the grain boundaries, open cracks are left behind in the grain boundary near the oxide-γFe interface because of the lack of supply of liquid phase. The enrichment of Sn in the liquid phase and the γFe phase would decrease the activity of Fe because Sn has less positive effects than Cu on the activity coefficient of Fe while comparing activity data for Fe-Cu and Fe-Sn systems at 1480 K (1207 °C) from literature.<sup>[53,54]</sup> To maintain the equilibrium between the wüstite layer and Fe, wüstite could decompose to release free oxygen. As the free oxygen diffuses down the open cracks, it could recombine to form oxygen molecules, and it is likely to react with Fe at the open crack surface where the Fe activity is high. The free oxygen could be used up in the open crack before reaching the liquid phase at the bottom of the crack in the grain boundaries, and therefore, oxides were found rarely beneath the liquid phase.

#### G. Effects of Sn on Oxidation Rate

As it is shown in Figure 4(b), the parabolic oxidation rates of Fe-Cu-Sn alloys were lower than the Fe and Fe-Cu cases but were slightly greater than the Fe-Cu-Ni alloy. The lower oxidation rates compared with Fe or Fe-Cu alloys did not likely result from (1) the formation of pores in the oxide layer because no pores were found; (2) the separation of oxides and metal during oxidation, which was validated by the wüstite thickness ratio being



around 95 pct (If oxides separate from metal during oxidation, then the wüstite thickness ratio would deviate from 95 pct distinctly); (3) the formation of Sn oxides because no Sn oxides were found. The separated liquid droplets on the interface were not likely to be responsible for the decrease in oxidation rate either because regions without liquid coverage would be enriched and form liquid phase again in a short time during the course of oxidation, and therefore, transport of Fe in those regions could not be interrupted. The decrease of Fe activity at the liquid-wüstite (or wüstite- $\gamma$ Fe if liquid is absent) interface could result in the change the transport of Fe through the wüstite layer, which most likely could be the reason why parabolic rates were lower than the Fe and Fe-Cu cases as proposed in a previous article for the Fe-Cu-Ni alloy.<sup>[17]</sup> An effort has been made to evaluate the activity of Fe in Cu-Sn liquid using the database that was used for constructing the Fe-Cu-Sn isotherm.<sup>[25]</sup> However, this resulted in an Fe activity around 0.95, and this value was even higher than the activity of Fe in the Cu liquid extrapolated from literature data,<sup>[55]</sup> which was not reasonable because, as mentioned before, Sn has less positive effect on the activity coefficient of Fe compared with Cu. Because independent experimental data on the activity data of Fe in the Cu-Sn liquid was not available to the authors' best knowledge, a quantitative analysis of parabolic rate constants for the Fe-Cu-Sn alloy was not conducted.

#### H. Summary of Effects of Sn

Sn has the following effects according to these results: (1) decrease oxidation rate; (2) maintain flat oxide- $\gamma$ Fe interface; (3) promote significant liquid penetration and grain-boundary broadening.

Although the presence of Sn could lower the oxidation rate, which would reduce the rejection of Cu, it does not decrease the amount of liquid phase at the oxide- $\gamma$ Fe interface because the liquid phase could incorporate a large amount of Sn and the back diffusion flux of Cu is smaller compared with Fe-Cu. Because Sn does not promote a wavy interface, it cannot promote occlusion of Cu-rich liquid into external oxides, which does not assist in suppressing hot shortness either. The most harmful effect is that Sn at contents as low as 0.03 wt pct promotes significant grain-boundary liquid penetration and broadening for only short-time exposure to the oxidizing atmosphere. The austenite grain boundary could be weakened significantly during the reheating process, and the cracks would propagate much deeper in the later rolling process, as reported by Imai *et al.* that the presence of Sn dramatically increases the number of surface cracks on steel after tensile deformation.<sup>[13]</sup>

Besides these detrimental effects, it was reported in the literature that Sn lowers the solubility of Cu in the  $\gamma$ Fe austenite phase<sup>[9]</sup> and lowers the melting point of the Cu-rich phase.<sup>[14]</sup> It also was noted that it required twice the amount of Ni to suppress surface hot shortness when 0.04Sn wt pct was added.<sup>[13,56]</sup>

In all, it is suggested that the content of Sn should be kept as low as possible to lower significantly liquid

penetration and crack formation in the grain boundaries, and lower the amount of Ni needed for suppressing surface hot shortness.

## IV. CONCLUSIONS

Short-time oxidation of a series Fe-Cu-Sn alloys were conducted in air at 1423 K (1150 °C) to investigate the effects of Sn for surface hot shortness. A numerical model developed in a previous article was applied to predict the liquid- $\gamma$ Fe interface concentration and interface morphology. The following are the conclusions of the study:

1. The model predicts liquid- $\gamma$ Fe interface concentrations at the liquid side and a flat  $\gamma$ Fe-oxide interface that agrees reasonably well with experimental SEM and SEM-EDS results.
2. The presence of Sn lowers the parabolic rate constants. This is likely a result of the enrichment of Sn in the liquid and  $\gamma$ Fe phase.
3. Sn promotes significant liquid penetration and cracks in grain boundaries, which could result from the fast diffusivity of Sn in the  $\gamma$ Fe grain boundary and the weak atomic Sn bonds.
4. Fe oxides were found at the open cracks in the grain boundary, which might result from the dissociation of the wüstite layer at the oxide- $\gamma$ Fe interface.

## ACKNOWLEDGMENTS

Financial support from the Center for Iron and Steelmaking Research (CISR) at Carnegie Mellon University is gratefully acknowledged. Discussions with Dr. Ron O'Malley at Nucor Steel and Professor Paul Wynblatt at Carnegie Mellon University are greatly appreciated.

## REFERENCES

1. Energetics Inc.: DOE/EE-0229, U.S. Department of Energy Office of Industrial Technologies, Washington, DC, 2000, pp. 10-16.
2. A. Nicholson and J.D. Murray: *J. Iron Steel Inst.*, 1965, vol. 203, pp. 1007-18.
3. D.A. Melford: *Phil. Trans. R. Soc. Lond.*, 1980, vol. 295 (1413), pp. 89-103.
4. J.K.S. Tee and D.J. Fray: *Ironmaking Steelmaking*, 2006, vol. 33 (1), pp. 19-23.
5. R.Y. Chen and W.Y.D. Yuen: *ISIJ Int.*, 2005, vol. 45 (6), pp. 807-16.
6. D.S. O'Neill: Ph.D. Dissertation, The University of New South Wales, Sydney, Australia, 2002.
7. B. Yalamanchili, P.M. Power, and J.B. Nelson: *Wire J. Int.*, 1999, vol. 32 (5), pp. 100-06.
8. K. Noro, M. Takeuchi, and Y. Mizukami: *ISIJ Int.*, 1997, vol. 37 (3), pp. 198-206.
9. W.J.M. Salter: *J. Iron Steel Inst.*, 1966, vol. 204, pp. 478-88.
10. T. Fukagawa and H. Fujikawa: *Oxid. Met.*, 1999, vol. 52 (3-4), pp. 177-94.
11. B.A. Webler, L. Yin, and S. Seetharaman: *Metall. Mater. Trans. B*, 2008, vol. 39B, pp. 725-37.
12. D.A. Melford: *J. Iron Steel Inst.*, 1962, vol. 200, pp. 290-99.



13. N. Imai, N. Komatsubara, and K. Kunishige: *ISIJ Int.*, 1997, vol. 37 (3), pp. 217–23.
14. G.G. Foster and J.K. Gilchrist: *Metallurgia*, 1952, vol. 225, p. 225.
15. W.J.M. Salter: *J. Iron Steel Inst.*, 1969, vol. 207, pp. 1619–23.
16. Y. Zou and E.W. Langer: *Mater. Sci. Eng. A*, 1989, vol. 110, pp. 203–08.
17. L. Yin, S. Balaji, and S. Sridhar: *Metall. Mater. Trans. B*, 2010, vol. 41B, pp. 598–611.
18. N. Birks, G.H. Meier, and F.S. Pettit: *High-Temperature Oxidation of Metals*, 2nd ed., Cambridge University Press, Cambridge, UK, 2006.
19. B.A. Webler and S. Sridhar: *Oxid. Met.*, 2009, vol. 71 (1–2), pp. 21–42.
20. Materials Preparation Center, Ames Laboratory: *U.S. Department of Energy Basic Energy Sciences*, [www.mpc.ameslab.gov](http://www.mpc.ameslab.gov).
21. K. Sachs and C.W. Tuck: *Proc. Conf. Reheating for Hot Working*, Iron and Steel Institute, Washington, DC, 1968.
22. H. Abuluwefa, R.I.L. Guthrie, and F. Ajersch: *Oxid. Met.*, 1996, vol. 46 (5–6), pp. 423–40.
23. W.S. Rasband: *ImageJ*, <http://rsb.info.nih.gov/ij/>, 1997.
24. Amiral: Version 3.1, Konrad-Zuse-Zentrum für Informationstechnik Berlin and Indeed, Visual Concepts GmbH, Berlin, Germany, 2003.
25. J. Miettinen: *CALPHAD*, 2008, vol. 32 (3), pp. 500–05.
26. Thermal-Calc Software AB: Version Q on WinNT, Stockholm, Sweden, 2004.
27. S. Pötschke and A.R. Buchner: *Steel Res. Int.*, 2006, vol. 77 (6), pp. 416–22.
28. M.M.G. Alemany, L.J. Gallego, L.E. Gonzalez, and D.J. Gonzalez: *J. Chem. Phys.*, 2000, vol. 113 (22), pp. 10410–11.
29. W.K. Chen and N.L. Peterson: *J. Phys. Chem. Solids*, 1975, vol. 36 (10), pp. 1097–103.
30. C.J. Smithells: in *Smithells Metals Reference Book*, 8th ed., W.F. Gale and T.C. Totemeier, eds., Elsevier Butterworth-Heinemann, Oxford, UK, 2004, pp. 13–22.
31. Y. Kondo: *ISIJ Int.*, 2004, vol. 44 (9), pp. 1576–80.
32. B.A. Webler and S. Sridhar: *ISIJ Int.*, 2008, vol. 48 (10), pp. 1345–53.
33. Comsol AB: FEMLAB Version 3.2, Reference manual, Stockholm, Sweden, 2005.
34. Matlab: MATLAB 7.0.4 Release 14, The Mathworks Inc., Natick, MA, 2005.
35. D.E. Coates and J.S. Kirkaldy: *J. Cryst. Growth*, 1968, vol. 3 (4), pp. 549–54.
36. R.Y. Chen and W.Y.D. Yuen: *Oxid. Met.*, 2003, vol. 59 (5–6), pp. 433–68.
37. L. Himmel, R.F. Mehl, and C.E. Birchenall: *J. Met.*, 1953, vol. 5 (6), pp. 827–43.
38. P. Wynblatt and M. Takashima: *Interface Sci.*, 2001, vol. 9 (3–4), pp. 265–73.
39. M. Hatano, K. Kunishige, and Y. Komizo: *Tetsu to Hagane*, 2002, vol. 88 (3), pp. 142–47.
40. E.E. Glickman and M. Nathan: *J. Appl. Phys.*, 1999, vol. 85 (6), pp. 3185–91.
41. D. Chatain, E. Rabkin, J. Derenne, and J. Bernardini: *Acta Mater.*, 2001, vol. 49 (7), pp. 1123–28.
42. C.S. Smith: *Trans. AIME*, 1948, vol. 175, pp. 15–51.
43. E. Pereiro-Lopez, W. Ludwig, and D. Bellet: *Acta Mater.*, 2004, vol. 52 (2), pp. 321–32.
44. K. Wolski, V. Laporte, N. Marie, and M. Biscondi: *Interface Sci.*, 2001, vol. 9 (3–4), pp. 183–89.
45. M.P. Seah and E.D. Hondros: *Proc. R. Soc. Lond. A Math.*, 1973, vol. 335 (1601), pp. 191–212.
46. J. Bernardini, P. Gas, E.D. Hondros, and M.P. Seah: *Proc. R. Soc. Lond. A Math.*, 1982, vol. 379 (1776), pp. 159–78.
47. V.A. Lazarev and V.M. Golikov: *Phys. Met. Metallogr. USSR*, 1971, vol. 31 (4), pp. 213–15.
48. H.S. Nam and D.J. Srolovitz: *Phys. Rev. B*, 2007, vol. 76 (18), pp. 184114-1–184114-14.
49. W. Sigle, G. Richter, M. Ruhle, and S. Schmidt: *Appl. Phys. Lett.*, 2006, vol. 89 (12), pp. 121911-1–121911-3.
50. E.O. Kirkendall: *Trans. AIME*, 1942, vol. 147, pp. 104–09.
51. E. Rabkin, L. Klinger, T. Izyumova, and V.N. Semenov: *Scripta Mater.*, 2000, vol. 42 (11), pp. 1031–37.
52. H. Fredriksson, K. Hansson, and A. Olsson: *Scand. J. Metall.*, 2001, vol. 30 (1), pp. 41–50.
53. M. Arita, M. Tanaka, K.S. Goto, and M. Someno: *Metall. Trans. A*, 1981, vol. 12 (3), pp. 497–504.
54. M. Arita, M. Ohyama, K.S. Goto, and M. Someno: *Z. Metallkd.*, 1981, vol. 72 (4), pp. 244–50.
55. U. Choudary, J. Serkin, and G. Belton: *Metall. Trans. B*, 1975, vol. 6B, pp. 399–403.
56. N. Imai, N. Komatsubara, and K. Kunishige: *ISIJ Int.*, 1997, vol. 37 (3), pp. 224–31.